Impurity seeding for suppression of the near Scrape-Off Layer heat flux feature in tokamak limited plasmas

F. Nespoli[1], B. Labit[1], I. Furno[1], C. Theiler[1], U. Sheikh[1], C.K. Tsui[1,2], J.A. Boedo[2], and the TCV team*

[1] *Ecole Polytechnique Fédérale de Lausanne (EPFL), Swiss Plasma Center (SPC), CH-1015 Lausanne, Switzerland*
[2] *University of California-San Diego, La Jolla, California 92093, USA*
* *See author list of S. Coda et al 2017 Nucl. Fusion 57 102011*
Email: nespolifederico@gmail.com

Abstract

In inboard-limited plasmas, foreseen to be used in future fusion reactors start-up and ramp down phases, the Scrape-Off Layer (SOL) exhibits two regions: the "near" and "far" SOL. The steep radial gradient of the parallel heat flux associated with the near SOL can result in excessive thermal loads onto the solid surfaces, damaging them and/or limiting the operational space of a fusion reactor. In this article, leveraging the results presented in [F. Nespoli et al., Nuclear Fusion 2017], we propose a technique for the mitigation and suppression of the near SOL heat flux feature by impurity seeding. First successful experimental results from the TCV tokamak are presented and discussed.

1 Introduction

Recent measurements in inboard-limited L-mode plasmas in many tokamaks [1, 2, 3, 4, 5, 6] with both infrared (IR) thermography and reciprocating Langmuir probes have revealed the presence of two regions in the Scrape-Off Layer (SOL): a "near" SOL, extending typically a few mm from the last closed flux surface (LCFS), characterized by a steep gradient of the parallel heat flux, and a "far" SOL, typically a few cm wide, featuring flatter heat flux profiles. The parallel heat flux radial profile in the SOL is then well described by a sum of two exponentials

$$q_{||}(r_u) = q_n \exp(-r_u/\lambda_n) + q_f \exp(-r_u/\lambda_f) \ , \tag{1}$$

where r_u is the upstream radial coordinate at the outer midplane, $r_u = 0$ at the LCFS, λ_n, λ_f are the parallel heat flux decay length in the near and far SOL, respectively, and q_n and q_f are the associated parallel heat flux magnitudes. An example of a typical parallel heat flux radial profile $q_{||}(r_u)$ described by Eq. (1) is shown in Fig. 1a with a solid line.
The near SOL is responsible for the peak heat loads on the limiter, that can be a factor of 6 higher [7] with respect to the value expected from the standard picture of the SOL [8], where only one decay length is assumed. Inboard limited L-mode plasmas are foreseen for future fusion reactor start-up and ramp-down phases. In ITER, the beryllium (Be) tiles covering the central column will act as a limiter. The ITER First Wall (FW) panels have been recently redesigned to handle the heat flux associated with the near SOL [7] that would otherwise exceed the Be tiles engineering constraint $q_{dep} \leq 4.7$ MWm^{-2}.
One can divide the power entering the SOL, P_{SOL}, into the contributions from the near and far SOL respectively, P_n and P_f, such that $P_{SOL} = P_n + P_f$. A schematic of this separation is depicted

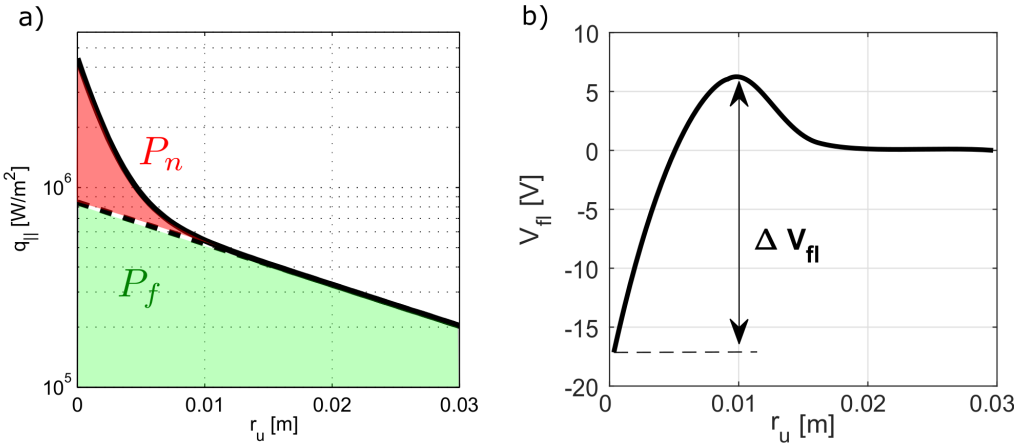

Figure 1: a) Schematic of a typical parallel heat flux radial profile $q_{||}(r_u)$ given by Eq. (1) (solid line). The dashed line represents the heat flux associated with the far SOL, $q_f \exp(-r_u/\lambda_f)$. The power entering the near and far SOL, P_n and P_f respectively, are given by the integral of the red and green shaded areas. b) Schematics of a typical floating potential radial profile $V_{fl}(r_u)$ from which the floating potential drop in the near SOL ΔV_{fl} is defined.

in Fig. 1a. We define power in the near SOL as

$$P_n = 4\pi R_{LCFS} \frac{B_{\theta,u}}{B_{\phi,u}} \int_0^\infty q_n e^{-r_u/\lambda_n} dr_u = 4\pi R_{LCFS} \frac{B_{\theta,u}}{B_{\phi,u}} q_n \lambda_n \ , \tag{2}$$

where R_{LCFS} is the major radius of the LCFS at the outer midplane, $B_{\theta,u}$ and $B_{\phi,u}$ are the poloidal and toroidal components, respectively, of the magnetic field at the outer midplane. Similarly, we compute the power into the far SOL as

$$P_f = 4\pi R_{LCFS} \frac{B_{\theta,u}}{B_{\phi,u}} q_f \lambda_f \ . \tag{3}$$

The physics of the near SOL in limited plasmas has been investigated in the TCV tokamak [9] at EPFL, Switzerland, with dedicated experiments detailed in Ref. [10]. The main results are summarized here:

- The power in the near SOL scales as $P_n \propto 1/\nu$, where $\nu = \dfrac{e n_e R_0 \eta_{||}}{m_i c_s}$ is the normalized Spitzer resistivity, with R_0 the plasma major radius, c_s the ion sound speed, $\eta_{||}$ the Spitzer resistivity [11], and all quantities are evaluated at the plasma edge.

- P_n vanishes at the limiter plates for $\nu \sim 7{\cdot}10^{-3}$, achieved by reducing the plasma current or by increasing the density, for values of the SOL collisionality ν^*_{SOL} corresponding to a conduction-limited regime, being $\nu^*_{SOL} = L/\lambda_{ee} \propto n_e T_e^{-2}$ [8] where $L = 2\pi R_0 q_a$ is the connection length, λ_{ee} is the electron-electron collisional mean free path and q_a is the safety factor at the LCFS.

- The near SOL heat flux feature disappears simultaneously at the limiter and at the outer midplane (OMP). Its poloidal asymmetry has been further investigated in Ref. [12].

- The near SOL heat flux feature is correlated with non-ambipolar currents flowing to the limiter [13], resulting in a drop of the floating potential profile $V_{fl}(r_u)$ near the contact point. The typical $V_{fl}(r_u)$ is schematized in Fig. 1b. Furthermore, P_n correlates with the magnitude of

the floating potential drop ΔV_{fl}, that can be considered as a proxy for the $\mathbf{E}\times\mathbf{B}$ shearing rate $\omega_{\mathbf{E}\times\mathbf{B}}$ in the near SOL. According to a recent theoretical model [14], the presence of a strong shear layer results in a steepening of the pressure profile, creating a separation in between near and far SOL. The shape of the typical V_{fl} profile has been recently explained in Ref. [15] as the result of the competition between the turbulence-driven polarization current and the poloidally asymmetric diamagnetic current, the former dominating in the near SOL. This theoretical model also predicts the progressive flattening of the V_{fl} profiles with increasing SOL collisionality (i.e. resistivity ν).

Based on the dependence of the power entering the near SOL upon the normalized resistivity $P_n \propto 1/\nu$ and its vanishing for high resistivity/collisionality, several methods could be envisaged to suppress the near SOL heat flux feature, or at least reduce it, and thus to prevent excessive inner wall heat loads in a future fusion reactor (ITER, DEMO...).
The mitigation of the near SOL heat flux by reducing the plasma current is not possible for a start-up scenario. Indeed, a minimum I_p is required to create a diverted configuration, which might not be low enough to prevent the formation of the near SOL. Increasing the density might not be a viable solution since wall pumping is usually strong during the start-up phase [16, 17], resulting in a rather low collisionality. Also, the heat flux on the limiter associated with the near SOL has been measured in TCV to first increase with n_e at low densities (sheath-limited regime), rolling over at intermediate densities (corresponding to the conduction limited regime) and eventually decreasing to negligible values for high densities, if this results in a sufficient drop of temperature along the field line [10]. Increasing the density could then increase the heat fluxes, reaching high heat loads that could damage the FW panels.
In this paper, we investigate the possibility to suppress the near SOL heat flux feature by reducing the SOL temperature, since $\nu \propto T_e^{-2}$. This can be done, for example, by increasing the radiated power P_{rad} via impurity seeding. Impurity seeding, routinely employed in divertor detachment experiments, has been extensively used in limited plasmas to cool the edge plasma and to increase confinement, e.g. in TEXTOR [18, 19, 20] and JET [21]. However, even if the presence of two scale lengths in the parallel heat flux at the limiter has been observed in these experiments [20], the effect of impurity seeding on the near SOL has never been investigated in the past. Furthermore, the possibility to use impurity seeding to fully suppress the near SOL heat flux feature has never been considered.

2 Experimental setup and and experiment overview

To test this hypothesis, a set of dedicated experiments have been performed in TCV, where the SOL plasma is cooled by the progressive injection of impurities. The radiator chosen for this experiment is N_2 because its radiation curve peaks around 10 eV [23], typically radiating mostly in the SOL and edge plasma, without significantly cooling the core plasma. The use of different radiators as Ne or Ar is also possible, and envisaged for further experiments.
An example discharge is #56142 (repeated in #56203 for diagnostics purposes). This is an ohmically heated deuterium plasma, and the main plasma parameters are $I_p = 140$ kA, $n_{e,av} = 2.5 \cdot 10^{19}$ m^{-3}, $\kappa = 1.4$, $\delta = 0$. The magnetic equilibrium reconstructed by the LIUQE code [22] is shown in Fig. 2 together with the main diagnostics used during the experiment, while the time evolution of the discharge is summarized in Fig. 3. While the plasma current I_p and averaged density $n_{e,av}$ are kept constant (Fig. 3a,b), together with the magnetic equilibrium, nitrogen (N_2) is injected through a piezoelectric valve located on the TCV floor (green rectangle in Fig. 2a). The nitrogen flow (in

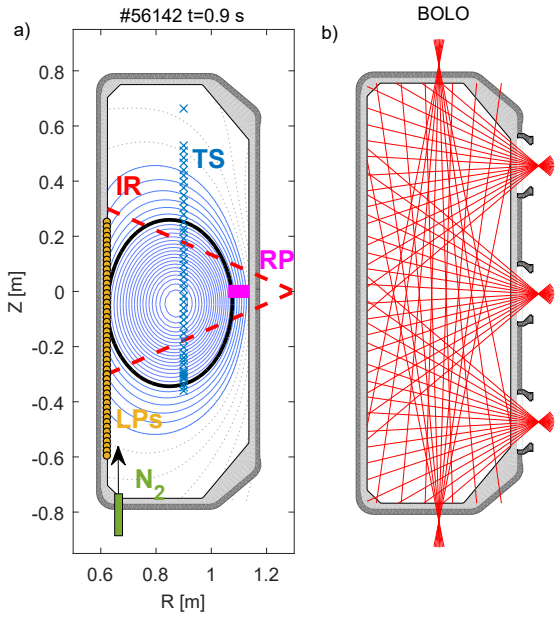

Figure 2: TCV cross section together with a) the magnetic equilibrium reconstruction provided by LIUQE [22], the IR camera field of view (red dashed lines), the location of the flush mounted LPs (orange dots) and of the TS measurements (blue crosses), the trajectory of the RP (magenta thick line), and the position of the valve used for N_2 injection (green rectangle) are also shown b) the 64 lines of sight of the bolometric system.

blue in Fig. 3c) is increased up to the constant level of $2 \cdot 10^{20}$ molecules/s, and then decreased back to zero, for a total of N_2 injected molecules corresponding to roughly 18% of the injected D_2 molecules (in red in Fig. 3c).
This leads to an increase of the plasma effective charge Z_{eff} (in red in Fig. 3d) by a factor 3 due to impurity penetration. Approximately 100 ms after the N_2 injection ends, Z_{eff} is decreased back to approximately 1.3 times its value before the N_2 injection, showing a slight accumulation of impurities. The plasma effective charge Z_{eff} is computed routinely in TCV by matching the plasma current using the ohmic and bootstrap current obtained from Ref. [24, 25], using n_e and T_e measurements from Thomson scattering (TS), and assuming stationary state. The loop voltage V_{loop} (in blue in Fig. 3d) exhibits a similar evolution, consistent with the changes in the plasma resistivity due to the variation of Z_{eff}.
Similarly, the total radiated power P_{rad} (in black in Fig. 3e) during the impurity seeding is increased by four times, and, after the N_2 injection ends, is decreased back to approximately 1.4 times its pre-seeding value. The power radiated in the SOL $P_{rad,SOL}$ and in the core $P_{rad,core}$ (in red and blue respectively in Fig. 3e) exhibit a similar evolution. P_{rad} and the plasma emissivity ϵ are computed from the tomographic inversion of 64 gold foil bolometers measurements, shown in Fig. 2b. Before the N_2 injection, ϵ is localized at the plasma contact point with the wall (Fig. 4a). During the impurity puff (Fig. 4b), the emissivity peaks below the contact point, consistently with the gas being injected from the bottom of the vessel. Also, ϵ is increased on the HFS part of the edge plasma, consistently with impurity penetration and with poloidal asymmetries in the impurity distribution previously observed in other tokamaks [26]. The emissivity in the core is less affected than in the edge plasma, the level of emitted radiation remaining unchanged for $\rho \leq 0.6$, where $\rho = \sqrt{[(\Psi - \Psi_{ax})/(\Psi_{LCFS} - \Psi_{ax})]}$ is the normalized flux coordinate, with Ψ the

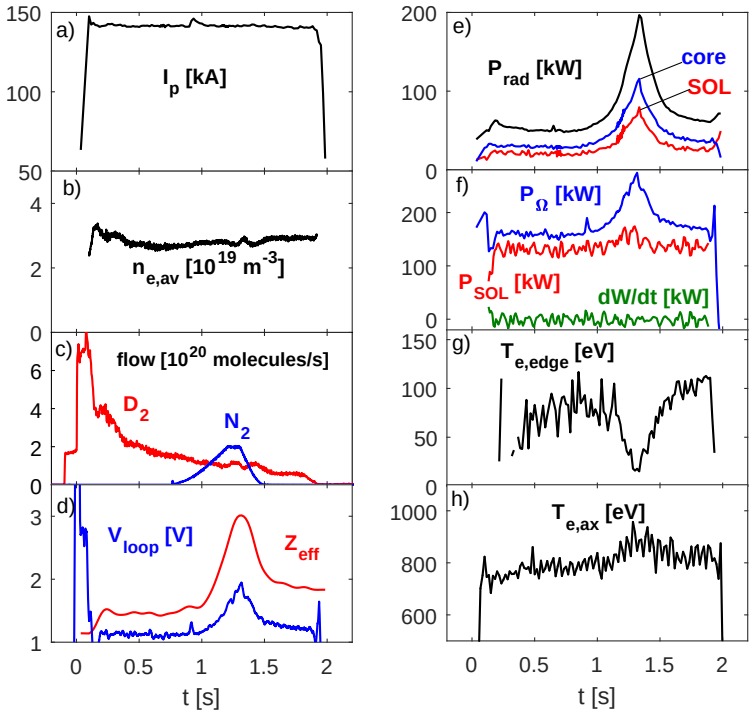

Figure 3: Time traces for discharge #56142 of a) plasma current I_p b) line-averaged electron density $n_{e,av}$ c) N_2 (blue) and D_2 (red) flow measured by the piezoelectric valve d) the plasma effective charge Z_{eff} (red) and the loop voltage V_{loop} (blue) e) total radiated power P_{rad} from bolometric measurements (black) with the contributions radiated inside (blue) and outside (red) the LCFS f) ohmic power P_Ω (blue), the power entering the SOL P_{SOL} (red) and the variation of the plasma total energy $\mathrm{d}W_E/\mathrm{d}t$ (green) g) electron temperature in the edge region $T_{e,edge}$ h) and on axis $T_{e,ax}$, form TS measurements.

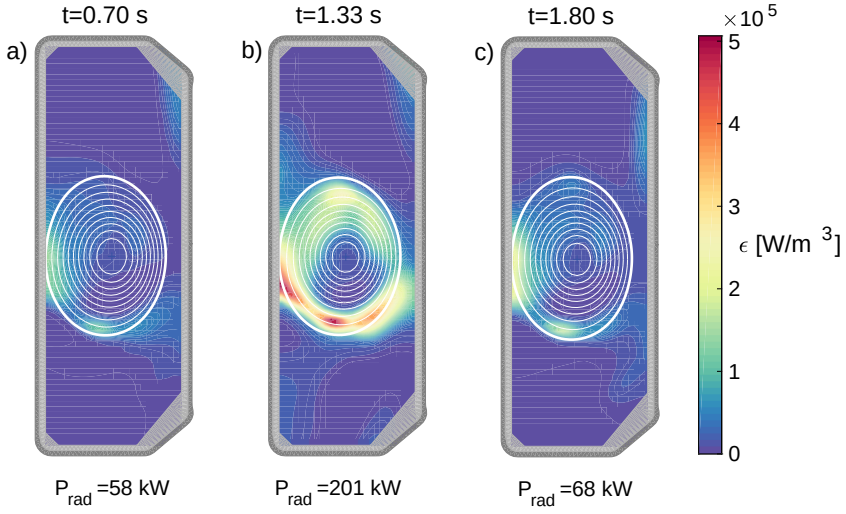

Figure 4: Plasma emissivity ϵ for discharge #56142 before (a), during (b) and after (c) N_2 injection, computed from the tomographic inversion of 64 gold foil bolometers measurements.

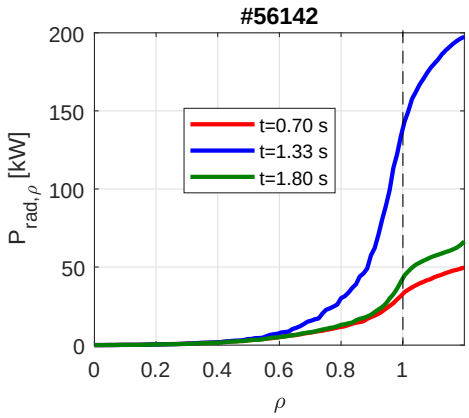

Figure 5: Power radiated inside each flux surface $P_{rad,\rho}$ for discharge #56142 before (red), during (blue) and after (green) N_2 injection. The LCFS ($\rho = 1$) is shown with a dashed line.

poloidal flux of the magnetic field, Ψ_{ax} and Ψ_{LCFS} its values on the magnetic axis and at the LCFS respectively. The formation of a "radiating mantle", similarly to the one observed in the TEXTOR experiments [18], is clearly shown in Fig. 5, where the power radiated inside each flux surface $P_{rad,\rho} = \iint \epsilon(R,Z)\Theta(\rho - \rho'(R,Z))2\pi R \mathrm{d}R\mathrm{d}Z$ is shown, with Θ the Heaviside step function. Also, after the N_2 injection, $P_{rad,\rho}$ is increased, with respect to the pre-seeding situation, only for $\rho > 0.9$. This suggests that the residual accumulation of impurities does not lower the main plasma temperature.

We remark that, as the radiated power is increased (Fig. 3e), the power entering in the SOL $P_{SOL} = P_\Omega - P_{rad,core} - \mathrm{d}W_E/\mathrm{d}t$ (in red in Fig. 3f) is not decreased, due to the increase of the ohmic power P_Ω (in blue in Fig. 3f) with Z_{eff}, V_{loop}, and to the negligible variation of the plasma total energy $\mathrm{d}W_E/\mathrm{d}t \sim 0$ (in green in Fig. 3f).

Consistently with the previously discussed results from bolometric measurements, Thomson scatter-

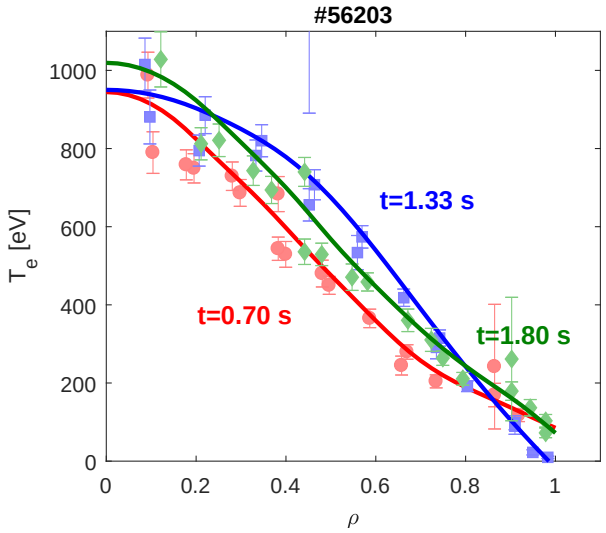

Figure 6: Electron temperature radial profile $T_e(\rho)$ from Thomson scattering measurements for discharge #56142 before (red circles), during (blue squares) and after (green diamonds) N_2 injection. Smooth interpolated profiles are plotted with solid lines.

ing measurements shows that the injection of N_2 results mainly in the cooling of the edge plasma. The electron temperature in the edge region $T_{e,edge} \equiv \langle T_e(\rho > 0.9)\rangle_\rho$ is decreased below 30 eV (Fig. 3g), while the electron temperature on the magnetic axis $T_{e,ax}$ (Fig. 3h) is slightly increased, resulting in the steepening of the temperature profile. After the N_2 injection, both $T_{e,edge}$ and $T_{e,ax}$ are increased with respect to their pre-seeding values by approximately 40% and 6%, respectively. The steepening of the temperature profile during impurity seeding, consistent with the results from previous seeding experiments in limited plasmas [18], and the following general increase of T_e, are more clearly shown in Fig. 6, where the radial profile of the electron temperature $T_e(\rho)$ is shown before (red), during (blue) and after (green) N_2 injection.
During the plasma discharge, three different diagnostics are used to characterize the near SOL. The temperature of the central column (CC) tiles is measured by and IR fast framing camera. Its detector is composed by 320×256 CdHgTe pixels, sensitive to the spectral range $4 < \lambda[\mu\text{m}] < 4.8$. The procedure used to compute the parallel heat flux radial profiles $q_{||}(r_u)$ is detailed in Ref. [10] and the main steps are summarized in the following. The heat flux deposited on the graphite tiles q_{dep} is evaluated using the THEODOR code [27], and is remapped onto the magnetic coordinates (r_u, α), where α is the angle between the magnetic field line and the plane tangent to the tile surface. The background and cross-field components of the heat flux, q_{BG} and $q_\perp(r_u)$ are evaluated. The parallel heat flux is finally computed inverting the relationship $q_{dep}(r_u, \alpha) = q_{||}(r_u)\sin\alpha + q_\perp(r_u)\cos\alpha + q_{BG}$. $q_{||}(r_u)$ is time averaged over time windows of 50 ms. The floating potential V_{fl} is measured by an array of flush-mounted Langmuir probes (LPs) embedded in the limiter. A reciprocating Langmuir probe (RP), is located at the outer midplane of the device and can perform up to two reciprocations during a discharge. The field of view of the IR camera, the position of the LPs and of the RP are shown in Fig. 2a.

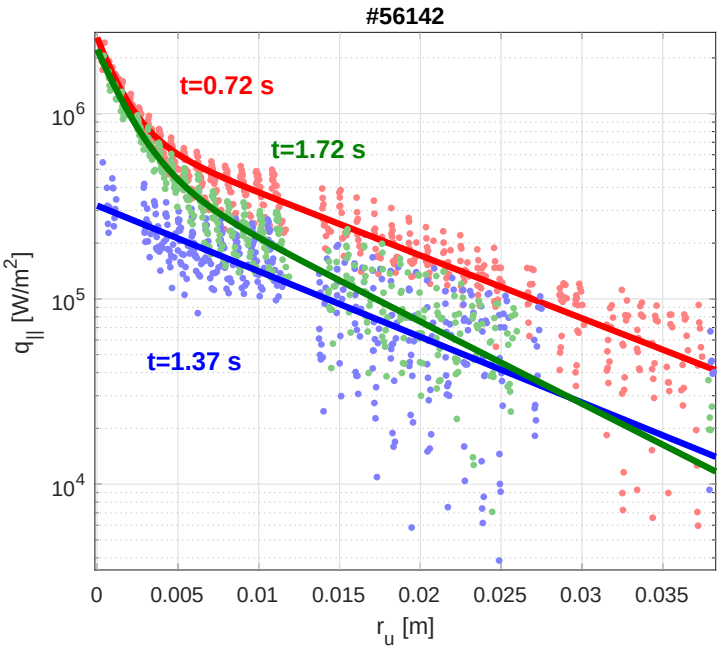

Figure 7: Parallel heat flux radial profiles $q_{||}(r_u)$ before N_2 injection (red dots), for $f_{rad} > 70\%$ (blue dots), and after the gas injection ends (green dots). The fit with Eq. (1) is shown with solid lines.

3 Suppression of near SOL heat flux feature and velocity shear layer

The parallel heat flux radial profile $q_{||}(r_u)$ before, during and after the N_2 injection are shown in Fig. 7 with red, blue and green dots, respectively. These profiles are fit to Eq. (1) to determine the physical parameters λ_n, q_n, λ_f and q_f. The result of the fit is shown in Fig. 7 with a solid lines. Before the gas injection, $q_{||}(r_u)$ exhibits a clear near SOL heat flux feature, with two different scale lengths for the near and far SOL. During the N_2 injection, the near SOL heat flux feature is suppressed and only one scale length is observed in the SOL. The near SOL heat flux feature is recovered after the end of the gas injection.

To better quantify the effect of N_2 injection on the heat flux at the limiter, we compute the power into the near and far SOL, P_n and P_f using Eqs. (2,3). The main results are exposed in Fig. 8 and are detailed in the following. In Fig. 8a, the radiated fraction $f_{rad} = P_{rad}/P_\Omega$ is shown, being P_Ω the ohmic power. The cooling of the plasma results in an increase of the normalized Spitzer

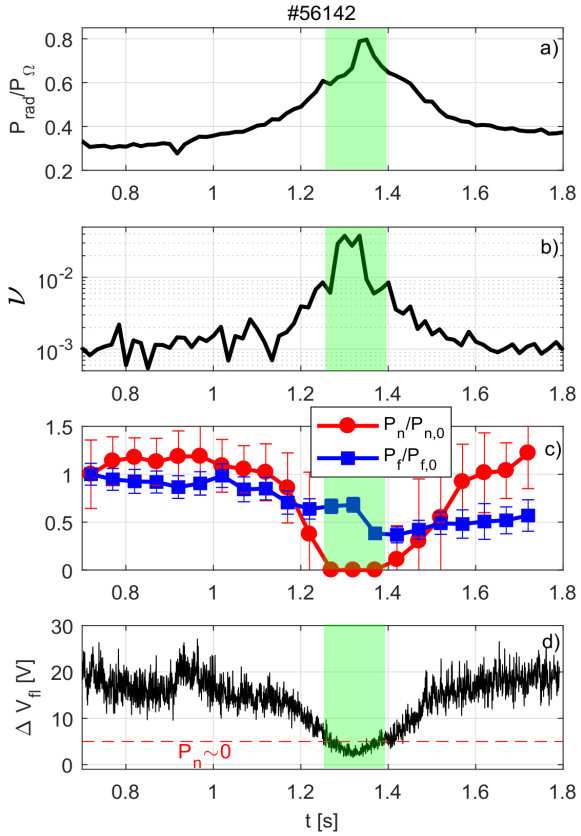

Figure 8: Time traces of a) radiated fraction $f_{rad} = P_{rad}/P_\Omega$ b) normalized Spitzer resistivity ν c) power into the near SOL P_n (red circles) and power into the far SOL P_f (blue squares), normalized to their values before N_2 injection, $P_{n,0}$ and $P_{f,0}$ d) drop in the floating potential ΔV_{fl} (black) compared to the value of ΔV_{fl} for which the near SOL feature is observed to disappear in TCV deuterium plasmas (dashed red line). The time window for which the near SOL is suppressed is depicted with a green shadowed region.

resistivity ν (Fig. 8b) above $7 \cdot 10^{-3}$, value for which the near SOL has been reported to disappear in TCV. The effect of the gas injection, resulting in the successful suppression of the near SOL heat flux feature, is evident from the vanishing of the power in the near SOL P_n at high values of f_{rad} (or ν). This is shown in Fig. 8c, where the time evolution of P_n and P_f, normalized to their values before the N_2 injection $P_{n,0}$ and $P_{f,0}$, are shown with red dots and blue squares, respectively. As the N_2 flow is increased, the power in the near SOL P_n decreases gradually and drops to zero when $f_{rad} \geq 60\%$. P_n recovers its initial value approximately 100 ms after the N_2 injection. The power in the far SOL P_f is less affected, being reduced only by 50%. Nevertheless, after the N_2 injection, P_f does not fully recover to the initial value. This is consistent with the residual presence of the "radiating mantle" in the outer edge and SOL region, as it emerges from bolometric measurements, resulting in a colder far SOL. We recall that, as discussed in section 2, the power entering the SOL P_{SOL} remains unchanged during the N_2 injection. Therefore, the decrease and eventual vanishing of P_n has to be considered the consequence of the increased radiation and plasma cooling in the SOL, and not of a decrease of P_{SOL} with the impurity seeding.
As it was shown in Refs. [10, 12], the near SOL heat flux feature vanishes at high resistivity not only at the limiter, but also at the outer midplane (OMP). This is also the case for this experiment. In Fig. 9, the $q_{||}(r_u)$ profiles (computed from T_e and I_{sat} measured by the RP with the methodology detailed in [12]) before and during the N_2 injection are shown in red and blue respectively for a typical discharge (#56203). These profiles rely on the magnetic reconstruction provided by LIUQE, for which the location of the LCFS at the OMP is affected by an uncertainty of a few mm. Even though no corrective shift as in Ref. [12] is applied, the final result remain unchanged: similarly to the heat flux profiles measured at the limiter, $q_{||}(r_u)$ before N_2 injection is well fit by a sum of two exponentials (Eq. 1, red thick line in Fig. 9). During the gas injection, the $q_{||}(r_u)$ profile in the SOL is sufficiently well described by a single exponential (blue solid line in Fig. 9).

In the following, we discuss LPs measurements of the floating potential V_{fl} at the limiter. This

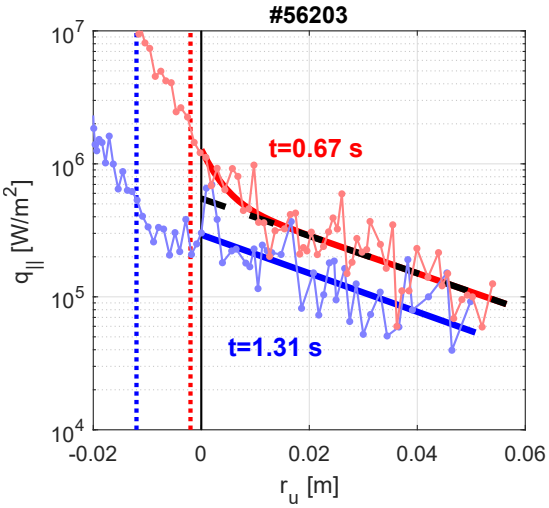

Figure 9: Radial profiles at the OMP of parallel heat flux $q_{||}(r_u)$, before N_2 injection (red) and for $f_{rad} > 60\%$ (blue). The fit of $q_{||}(r_u)$ with Eq. (1) is shown with thick lines, while the heat flux associated with the far SOL $q_{||,f}(r_u) = q_f \exp(r_u/\lambda_f)$ is shown with a black dashed line for the case before N_2 injection. The LCFS position from LIUQE is marked by a black vertical line. The LCFS location according to the method used in Ref. [12] is shown with vertical dotted lines.

has a two-fold motivation: first, confirming the suppression of the near SOL as it appears from IR measurements; secondly, we propose the V_{fl} measurements as a trigger for an actuator for real time monitoring of the presence of the near SOL in a start-up phase limited plasma.
Indeed, as discussed in section 1, the presence of near SOL steep gradients is correlated with the presence of local non-ambipolar currents flowing to the limiter [13, 15]. These currents cause, in TCV limited plasmas, a drop in the floating potential radial profiles $V_{fl}(r_u)$ at the limiter, measured with LPs, that reach strong negative values as one approaches the LCFS. A V_{fl} profile in the direction along the limiter before N_2 injection is shown with red dots in Fig. 10.
Following Ref. [10], we consider the drop in the floating potential $\Delta V_{fl} \equiv V_{fl,max} - V_{fl,min}$, with $V_{fl,max}$ and $V_{fl,min}$ the maximum and minimum value of V_{fl}, here evaluated on the electron drift-side of the limiter, as a proxy the $\mathbf{E} \times \mathbf{B}$ shearing rate. In Fig. 8d, the time evolution of ΔV_{fl} is plotted in black, and compared with the value $\Delta V_{fl} = 5$ V, for which the power in the near SOL P_n has been previously reported to vanish in TCV deuterium plasmas [10]. As the gas injection progresses, the ΔV_{fl} is reduced, reaching values below 5 V, corresponding to a low $\omega_{\mathbf{E}\times\mathbf{B}}$, which according to the model in Ref. [14] would be no longer sufficient to change the turbulence and create the separation in between near and far SOL. A V_{fl} profile corresponding to this phase is shown with blue squares in Fig. 10. As the N_2 injection ends, ΔV_{fl} recovers its initial value and the previous shear layer is restored (green diamonds in Fig. 10).
The V_{fl} measurements from flush mounted LPs provide a reliable indication of the presence of a near SOL heat flux feature. These do not require an elaborated analysis, like for the IR camera, and it can produce reliable results immediately after each discharge, or even in real time, and could therefore be used as a trigger for an actuator during the start-up and ramp-down phases. For this purpose, if one already knows the position of the plasma, only measurements from two different probes for each limiter side are needed. Otherwise, to correctly identify the maximum of V_{fl}, at least four probes per limiter side could be needed. We remark that this technique is somehow similar to

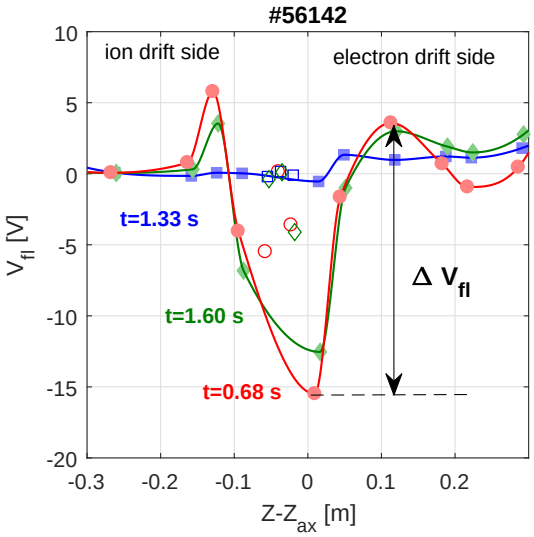

Figure 10: Floating potential profile along the direction of the limiter, $Z - Z_{ax}$, with Z_{ax} the vertical position of the plasma magnetic axis, before N_2 injection (red dots), for $f_{rad} > 60\%$ (blue squares) and after the gas injection end (green diamonds). The profiles are interpolated with cubic splines. The drop in the floating potential ΔV_{fl} is shown. Measurements from LPs shaded by the neighboring tiles are plotted with open symbols.

the one used in ASDEX-U to detect detachment, where the thermoelectric current flowing to the divertor plate is measured with a single shunt, and used as a proxy of the heat flux deposited on the divertor plate [28].

4 Implications for plasma start-up phase in a fusion reactor

The main drawback of our method is the transient increase in plasma resistance, which might increase the poloidal magnetic flux consumption during the start-up phase, Φ_{tot}. This quantity is indeed of great importance for the design and operation of a fusion reactor, since it determines both the size of the central solenoid for a steady state tokamak during its design phase [29], and the duration of the inductive part of a plasma discharge. The total poloidal flux consumption can be decomposed as [29] $\Phi_{tot} = \Phi_{ext} + \Phi_{int} + \Phi_{res}$, where Φ_{ext} and Φ_{int} are the external and internal inductive flux consumption due to the plasma current outside and inside the LCFS, and are fixed by the plasma shape and current and by the current profile, respectively. Φ_{res} is the resistive flux consumption due to the resistive dissipation of magnetic energy, and can be expressed as [29, 30, 31]

$$\Phi_{res} = \int_{t_0}^{t1} \frac{dt}{I_p} \int j_\phi E_\phi dV = \int_{t_0}^{t1} dt R_\Omega I_p = \int_{t_0}^{t1} dt V_{loop} \, , \tag{4}$$

where t_0 and t_1 are the beginning and ending times of the current ramp-up, j_ϕ and E_ϕ are the toroidal plasma current density and the toroidal electric field, R_Ω is the total plasma resistance, I_p is the plasma current and V_{loop} is the loop voltage. The last two equalities of eq.(4) make it clear that Φ_{res} is proportional to the time integral of the plasma resistivity (or effective charge Z_{eff}). The increase of ν due to the impurity injection would therefore cause an increase in Φ_{res}. However, a more resistive plasma leads to a shorter current penetration time. This allows a higher current ramp rate, which is limited by the rising of MHD instabilities [32]. A faster current ramp would in turns decrease the flux consumption Φ_{tot} allowing a reduction of t_1 in eq. (4). As it was shown in Ref. [32], both effects would balance out leaving the total flux consumption unchanged within a few percent or less as the plasma resistivity is increased.
Moreover, Φ_{res} can be reduced by the use of non-inductive current sources. Start up scenarios with reduced flux consumption have been planned using neutral beam [33] and electron cyclotron [29] current drive for JT60-SA and DEMO respectively. Current drive sources could then be used in a fusion reactor together with impurity injection to mitigate the heat fluxes on the limiter without increasing Φ_{res}.
Finally, we remark that it is also possible to calibrate the level of injected impurity, used in this work to suppress the near SOL heat flux feature, to just reduce the deposited near SOL heat flux under the engineering constraints (4.7 MW/m^2 for ITER FW Be panels [7]) without completely suppressing it, while keeping a sufficiently low plasma resistance during the start-up phase.

5 Conclusion

Concluding, leveraging the results from previous experiments in TCV, a method based on impurity seeding to suppress the near SOL heat flux feature has been proposed and tested. The results from the IR together with LPs measurements show that the near SOL heat flux at the limiter is successfully suppressed by N_2 injection for $f_{rad} > 60\%$, and the initial situation is almost restored after the gas injection. The increase of Z_{eff} of $\sim 30\%$ with respect to its initial value showing a slight accumulation of impurities in the main plasma. RP measurements show that the near SOL heat flux feature is successfully suppressed at the OMP as well. Also, we demonstrate how LPs

embedded in the limiter are a reliable diagnostic to monitor the presence of a near SOL through V_{fl} measurements.
The extrapolation of impurity transport, whose analysis is beyond the objectives of this work, from TCV to an ITER-scale fusion reactor is difficult, and similar experiments would be needed to be performed in bigger tokamaks featuring metallic walls to better assess the applicability of the method proposed in this paper to a reactor of the size of ITER or DEMO. Still, the modest pollution of the main plasma after the end of the gas injection might render this mitigation method suitable for a start-up phase in a fusion reactor. Furthermore, bolometric measurements show that the injected impurity radiate mainly in the outer edge plasma and the SOL, creating a "radiating mantle", still present after the end of the N_2 injection, even with substantially lower f_{rad}. This has a twofold beneficial effect of both decreasing the heat flux in the far SOL, as shown from IR measurements, and to increase the main plasma temperature, as shown by Thomson scattering measurements.
The effect of impurity seeding on the poloidal magnetic flux consumption during the start-up phase Φ_{tot} has been discussed. The value of Φ_{tot} could be kept unchanged even during impurity seeding by one or more of the following: i) the increase of the plasma ramp-up rate allowed by the increased plasma resistivity ii) the use of non inductive current sources iii) the tuning of the injected impurity level for keeping the deposited heat flux on the limiter below the engineering limits without totally suppressing the near SOL heat flux feature.

Acknowledgments

This work has been carried out within the framework of the EUROfusion Consortium and has received funding from the Euratom research and training programme 2014-2018 under grant agreement No 633053. The views and opinions expressed herein do not necessarily reflect those of the European Commission. This work was supported by the U.S. Department of Energy under Grant No. DE-SC0010529.

References

[1] G. Arnoux T. Farley, C. Silva, S. Devaux, M. Firdaouss, D. Frigione, R. Goldston, J. Gunn, J. Horacek, S. Jachmich, P.J. Lomas, S. Marsen, G.F. Matthews, R.A. Pitts, M. Stamp, P. Stangeby and JET EFDA contributors. **Scrape-off layer properties of ITER-like limiter start-up plasmas in JET**. *Nuclear Fusion*, **53**:073016, 2013.

[2] F. Nespoli B. Labit I. Furno G.P. Canal A. Fasoli. **Heat loads in inboard-limited L-mode plasmas in TCV**. *Journal of Nuclear Materials*, **463**:393–396, 2015.

[3] J. Horacek, P. Vondracek, R. Panek, R. Dejarnac, M. Komm, R.A. Pitts, M. Kocan, R.J. Goldston, P.C. Stangeby, E. Gauthier, P. Hacek, J. Havlicek, M. Hron, M. Imrisek, F. Janky, J. Seidl . **Narrow heat flux channels in the COMPASS limiter scrape-off layer**. *Journal of Nuclear Materials*, **463**:385–388, 2015.

[4] P.C. Stangeby, C.K. Tsui, C.J. Lasnier, J.A. Boedo, J.D. Elder, M. Kocan, A.W. Leonard, A.G. Mclean, R.A. Pitts, D.L. Rudakov. **Power deposition on the DIII-D inner wall limiter**. *Journal of Nuclear Materials*, **463**:389–392, 2015.

[5] E.S. Marmar, S.G. Baek, H. Barnard, P. Bonoli, D. Brunner, J. Candy, J. Canik, R.M. Churchill, I. Cziegler, G. Dekow et al. . **Alcator C-Mod: research in support of ITER and steps beyond** . *Nuclear Fusion*, **55**:104020, 2015.

[6] J.G.Bak R.A.Pitts H.S.Kim H.H.Lee C.Bin J.W.Juhn S.H.Hong O.E.Garcia R.A.Kube D.C.Seo . **Measurement of inner wall limiter SOL widths in KSTAR tokamak**. *Nuclear Materials and Energy*, **article in press**, 2016.

[7] M. Kocan, R.A. Pitts, G. Arnoux, I. Balboa, P.C. de Vries, R. Dejarnac, I. Furno, R.J. Goldston, Y. Gribov, J. Horacek, et al. **Impact of a narrow limiter SOL heat flux channel on the ITER first wall panel shaping**. *Nuclear Fusion*, **55**:033019, 2015.

[8] P.C. Stangeby. **The Plasma Boundary of Magnetic Fusion Devices** . *Institute of Physics Publishing Bristol and Philadelph*, 2000.

[9] S. Coda, J. Ahn, R. Albanese, S. Alberti, E. Alessi, S. Allan, H. Anand, G. Anastassiou, Y. Andrebe, C. Angioni, et al. **Overview of the TCV Tokamak Program: Scientific Progress and Facility Upgrades**. *Nuclear Fusion*, **57**:102011, 2016.

[10] F. Nespoli, B. Labit, I. Furno, J. Horacek, C.K. Tsui , J.A. Boedo, R. Maurizio, H. Reimerdes, C. Theiler, P. Ricci, F.D. Halpern, U. Sheikh, K. Verhaegh, R.A. Pitts, F. Militello, The EUROfusion MST1 Team and The TCV Team. **Understanding and suppressing the near Scrape-Off Layer heat flux feature in inboard-limited plasmas in TCV**. *Nuclear Fusion*, **57** :126029, 2017.

[11] R.J. Goldston and P.H. Rutherford. **Introduction to Plasma Physics**. *Bristol: Institute of Physics Publishing*, 1997.

[12] C. K. Tsui, J. A. Boedo, F. D. Halpern, J. Loizu, F. Nespoli, J. Horacek, B. Labit, J. Morales, H. Reimerdes, P. Ricci, C. Theiler, S. Coda, B. P. Duval, I. Furno, TCV Team, and EUROfusion MST1 Team. **Poloidal asymmetry in the narrow heat flux feature in the TCV scrape-off layer**. *Physics of Plasmas*, **24**:062508, 2017.

[13] R. Dejarnac, P.C. Stangeby, R.J. Goldston, E. Gauthier, J. Horacek, M. Hron, M. Kocan, M. Komm, R. Panek, R.A. Pitts, P. Vondracek. **Understanding narrow SOL power flux component in COMPASS limiter plasmas by use of Langmuir probes**. *Journal of Nuclear Materials*, **463**:381–384, 2015.

[14] F. D. Halpern and P. Ricci. **Velocity shear, turbulent saturation, and steep plasma gradients in the scrape-off layer of inner-wall limited tokamaks**. *Nuclear Fusion*, **57**:034001, 2017.

[15] J. Loizu, J. A. Morales, F. D. Halpern, P. Ricci, P. Paruta. **Scrape-off-layer current loops and floating potential in limited tokamak plasmas**. *Journal of Plasma Physics*, **83**:57583601, 2017.

[16] V. Philipps T. Loarer H.G. Esser S. Vartanian U. Kruezi S. Brezinsek G. Matthews. **Dynamic fuel retention and release under ITER like wall conditions in JET**. *Journal of Nuclear Materials*, **438**:S1067–S1071, 2013.

[17] M Mayer V Philipps P Wienhold H.G Esser J von Seggern M Rubel. **Hydrogen inventories in nuclear fusion devices**. *Journal of Nuclear Materials*, **290-293**:381–388, 2001.

[18] U. Samm , G. Bertschinger, P. Bogen, J.D. Hey, E. Hintz, L. Konen, Y.T. Lie, A. Pospieszczyk, D. Rusbuldt, R.P. Schorn, B. Schweer, M. Tokar, B. Unterberg. **Radiative edges under control by impurity fluxes**. *Plasma Physics and Controlled Fusion*, **35**, 1993.

[19] Messiaen, A. M. Ongena, J. Samm, U. Unterberg, B. Van Wassenhove, G. Durodie, F. Jaspers, R. Toka, M. Z. Vandenplas, P. E. Van Oost, G. Winter, J. et al. **High confinement and high desnity with stationary plasma energy and strong edge radiation in the TEXTOR-94 tokamak**.

[20] K.H. Finken T. Denner and G. Mank. **Thermal load distribution on the ALT-II limiter of TEXTOR-94 during RI mode operation and during disruptions**. *Nuclear Fusion*, **40**:339, 2000.

[21] G.P. Maddison, M. Brix, R. Budny, M. Charlet, I. Coffey, J.G. Cordey, P. Dumortier, S.K. Erents, N.C. Hawkes, M. von Hellermann, D.L. Hillis, J. Hogan, L.D. Horton, et al. **Impurity-seeded plasma experiments on JET**. *Nuclear Fusion*, **43**:49–62, 2003.

[22] F. Hofmann and G. Tonetti. **Tokamak equilibrium reconstruction using Faraday rotation measurements**. *Nuclear Fusion*, **28**:1871–1878, 1988.

[23] A. Kallenbach , M. Balden , R. Dux , T. Eich , C. Giroud , A. Huber , G.P. Maddison , M. Mayer , K. McCormick , R. Neu, et al. **Plasma surface interactions in impurity seeded plasmas**. *Journal of Nuclear Materials*, **415**:S19–S26, 2011.

[24] O. Sauter and C. Angioni. **Neoclassical conductivity and bootstrap current formulas for general axisymmetric equilibria and arbitrary collisionality regime**. *Physics of Plasmas*, **6**:2834, 1999.

[25] O. Sauter and C. Angioni. **Erratum: Neoclassical conductivity and bootstrap current formulas for general axisymmetric equilibria and arbitrary collisionality regime**. *Physics of Plasmas*, **9**:5140, 2002.

[26] R.M. Churchill, B. Lipschultz, C. Theiler and the Alcator C-Mod Team. **In-out impurity density asymmetry in the pedestal region of Alcator C-Mod**. *Nuclear Fusion*, **53**:122002, 2013.

[27] A. Herrmann. **Limitations for divertor heat flux calculations of fast events in tokamaks**. *ECA*, **25A**:2109–2112, 2001.

[28] A. Kallenbach, M. Bernert, M. Beurskens, L. Casali, M. Dunne, T. Eich, L. Giannone, A. Herrmann, M. Maraschek, S. Potzel, et al. **Partial detachment of high power discharges in ASDEX Upgrade**. *Nuclear Fusion*, **55**, 2015.

[29] T. Wakatsuki, T. Suzuki, N. Hayashi, J. Shiraishi, Y. Sakamoto, S. Ide, H. Kubo and Y. Kamada. **Reduction of poloidal magnetic flux consumption during plasma current ramp-up in DEMO relevant plasma regimes**. *Nuclear Fusion*, **57**:016015, 2017.

[30] S. Ejima, R.W. Callis, J.L. Luxon, R.D. Stambaugh, T.S. Taylor and J.C. Wesley. **Volt-second analysis and consumption in Doublet III plasmas**. *Nuclear Fusion*, **22**:1313, 1982.

[31] J.E. Menard, B.P. LeBlanc, S.A. Sabbagh, M.G. Bell, R.E. Bell, E.D. Fredrickson, D.A. Gates, S.C. Jardin, D.W. Johnson, S.M. Kaye, et al. **Ohmic flux consumption during initial operation of the NSTX spherical torus**. *Nuclear Fusion*, **41**:1197, 2001.

[32] S.C. Jardin, C.E. Kessel and N. Pomphrey. **Poloidal flux linkage requirements for the International Thermonuclear Experimental Reactor**. *Nuclear Fusion*, **34**:1145, 1994.

[33] T Wakatsuki, T Suzuki, N Hayashi, J Shiraishi, S Ide and Y Takase. **Simulation of plasma current ramp-up with reduced magnetic flux consumption in JT-60SA**. *Plasma Physics and Fusion*, **57**:065005, 2015.